J Mater Sci: Mater Electron (2015) 26:1619–1624
DOI 10.1007/s10854-014-2585-8

Enhancement of Seebeck coefficient in Sb-rich Sb_2Te_3 thin film

Ziqiang Zhang · Yigui Wu · Haiming Zhang · Zhigang Zeng · Zhiyu Hu

Received: 29 September 2014 / Accepted: 5 December 2014 / Published online: 23 January 2015
© Springer Science+Business Media New York 2015

Abstract The influence of excess antimony (Sb) on the Seebeck coefficient of antimony telluride (Sb_2Te_3) was investigated. Sb-rich Sb_2Te_3 thin film experimentally acquires Seebeck coefficient of 536 μV K^{-1} at room temperature, almost six times of stoichiometric Sb_2Te_3 thin film 90 μV K^{-1}. The prominent enhancement of Seebeck coefficient could be attributed to carrier energy filtering effect at Sb/Sb_2Te_3 nanocrystal boundaries, evidenced by a set of characterizations. Meanwhile, Sb-rich Sb_2Te_3 thin film behaves low thermal conductivity. This experiment result implies that by altering Sb content, various Seebeck coefficients would be acquired in Sb-rich Sb_2Te_3 films. The highly thermoelectricity performance is especially appropriate for thermo-electric device such as thermoelectric sensor.

Z. Zhang · H. Zhang · Z. Hu (✉)
School of Materials Science and Engineering, Shanghai University, Shanghai 200072, China
e-mail: zhiyuhu@shu.edu.cn

Z. Zhang · Y. Wu · H. Zhang · Z. Zeng · Z. Hu
Institute of NanoMicroEnergy, Shanghai University, Shanghai 200444, China

Y. Wu · Z. Zeng · Z. Hu
Department of Physics, Shanghai University, Shanghai 200444, China

Z. Hu
Department of Chemistry, Shanghai University, Shanghai 200444, China

Z. Hu
Research Institute of Micro/Nano Science Technology, Shanghai Jiao Tong University, Shanghai 200240, China

1 Introduction

Thermoelectric (TE) materials are one of important function materials, which can realize the conversion of heat into electricity silently, or vice versa, based on Seebeck effect or Peltier effect. The efficiency of TE materials is characterized by the dimensionless figure of merit ZT, which is defined as $ZT = S^2\sigma_H T/\kappa$, where S, σ, T and κ are Seebeck coefficient or thermopower), electrical conductivity, absolute temperature and thermal conductivity, respectively. The excellent TE materials with high ZT should possess high power factor P ($P = S^2\sigma$) and low thermal conductivity (κ). To optimize ZT performance is a complex project, as the interdependence of the Seebeck coefficient, electrical conductivity, and thermal conductivity. So far, remarkable advances in ZT have been acquired in different material systems by implantation of various nanostructures into materials, for example, nanocomposites [1], nanowire [2], quantum dot superlattices [3]. In these materials, the enhancement of ZT is mainly achieved through the large reduction of thermal conductivity due to phonon scattering by interfaces and/or boundaries. However, the improvement of ZT through elevating power factor is relatively rarely [4]. To enhance power factor, seen from its definition ($S^2\sigma$), we need increase S and σ simultaneously, or improve S remarkably yet not lead σ to decrease obviously. One of the effective methods to elevate S is the density of states increase due to the formation of a resonance state [5]. On the other hand, S enhancement can also be attained by a carrier energy filtering effect, caused by band bending at the interfaces between nanoinclusions and TE host materials [4, 6–9].

Sb_2Te_3 and its derivatives are considered to be one of the best p-type TE materials at the room temperature. Herein, we present experimental evidence of S enhancement in Sb-rich

Sb_2Te_3 films. To our knowledge, there is not report about the result. This similar phenomenon has also been described in Pb-rich PbTe sample [7]. Our results show that the Sb-rich film holds Seebeck coefficient of 536 $\mu V\ K^{-1}$ at room temperature, almost six times of stoichiometric Sb_2Te_3 thin film 90 $\mu V\ K^{-1}$. The increase on Seebeck coefficient is attributed to carrier potential barrier formed at interfaces of Sb–Sb_2Te_3 as a carrier filter, separating carriers with different energy. X-ray diffraction (XRD) patterns show the Sb-rich Sb_2Te_3 sample direct deposition is polycrystal and displays the presence of metallic Sb. The presence of Sb–Sb_2Te_3 interfaces is demonstrated by transmission electron microscopy (TEM) characterization. The cross-plane thermal conductivity measurement using a differential 3ω technique reveals Sb–Sb_2Te_3 sample behaves low thermal conductivity. Our experiment results imply that by altering Sb content, various Seebeck coefficients would be acquired in Sb-rich Sb_2Te_3 films. The prominent thermopower makes it possible for use on thermo-electric devices such as TE sensor [10].

2 Experimental

In this work, antimony tellurium films were deposited using method of co-evaporation of antimony and tellurium materials onto a well cleaned quartz glass substrate at room temperature (~300 K) using a molecular beam epitaxy (MBE) system. High-purity (99.999 %) materials of antimony and tellurium were evaporated independently from effusion cells in a high vacuum chamber at 10^{-9} Torr.

The power applied to each effusion cell was controlled separately. Two proportional-integral-derivative controllers were used to maintain the effusion cell temperature and the material deposition rate at fixed values during the film growth. The deposition rate and the film thickness were monitored by a quartz crystal oscillator. During the process, we maintained the Te evaporation rate on 0.8 $\mathrm{\AA\ s^{-1}}$ with effusion cell temperature about 568 K, then changing the Sb evaporation rates at the range of 0.4–0.6 $\mathrm{\AA\ s^{-1}}$. The rate values were set according to theory calculation and experience to ensure the Sb to Te ratio being nearly 2:3. Sample 1 (S1), sample 2 (S2) and sample 3 (S3) with thickness of ~200 nm were acquired when Sb evaporation rates were 0.4, 0.5 and 0.6 $\mathrm{\AA\ s^{-1}}$, respectively.

The chemical compositions of the films were analysed employing energy dispersive X-ray spectroscopy (EDS) (ZEISS ULTRA55, Germany). The crystal structures of the films were characterized using XRD (D/MAX-2200, Japan). The sample thicknesses were measured once more by step profiler (Amboise XP-200, America). The morphology analysis was performed on TEM (JEM-2010F, Japan).

The information of the carrier concentration, mobility and derivate electrical conductivity was obtained at room temperature by the Hall coefficient (HL5500, Britain) measurement. The electrical conductivity of the specimens at room temperature was also evaluated by four-probe method. For TE property, the Seebeck coefficient in-plane was obtained by a laboratory-designed apparatus at room temperature as shown in Fig. 1 [11]. By controlling the electric current, the heater and the cooler could provide varying temperature. One side of the specimen was putted on the heater, the other side on the cooler to build the temperature difference along the specimen. The induced thermal voltage and the real-time temperature monitored by thermocouples (OMEGA, USA) were collected by a data acquisition unit (34970, Agilent, USA). The Seebeck voltage (ΔV) as a function of temperature difference (ΔT, below 5 K) gave a straight line and the slope was the Seebeck coefficient. The cross-plane thermal conductivity was measured using a differential 3ω technique. The 3ω technique in detail could be found in other reports [12, 13]. For preparation, a ~200 nm thickness SiO_2 insulating layer was grown on the sample. By a standard lift-off process, a thin silver wire was deposited on the insulating layer surface.

3 Results and discussion

The chemical compositions of the samples as deposited are analysed employing EDS analysis (Fig. 2). With the increase of Sb evaporation rate, Sb atomic percentage varies monotonely from Sb-poor to Sb-rich. At the Sb evaporation rate of 0.5 $\mathrm{\AA\ s^{-1}}$, atomic composition of the film is close to stoichiometry (Sb_2Te_3, sample S2). However, at the Sb evaporation rate of 0.6 $\mathrm{\AA\ s^{-1}}$, Sb atomic content increases drastically to ~63 % (sample S3).

The crystallinity of the films as deposited is investigated by XRD (Fig. 3). All the samples are polycrystalline. The crystallinity of sample S1 is better than S2 and S3. The main peaks in all samples could be indexed to rhombohedral phase (JCPDS 15-0874, $R\bar{3}m$). Thus a structure which

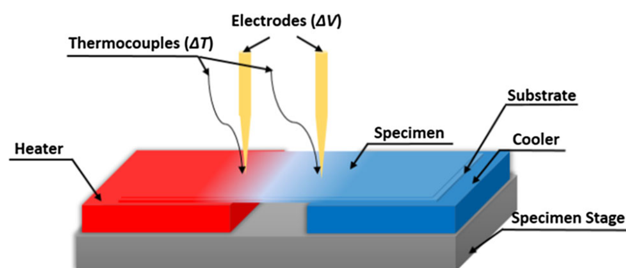

Fig. 1 Schematic of experimental set-up for Seebeck coefficient measurement

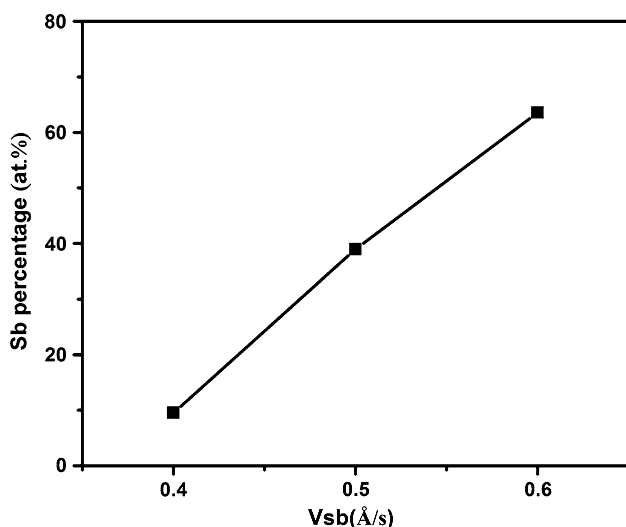

Fig. 2 Sb atomic percentage in different samples as a function of Sb evaporation rate

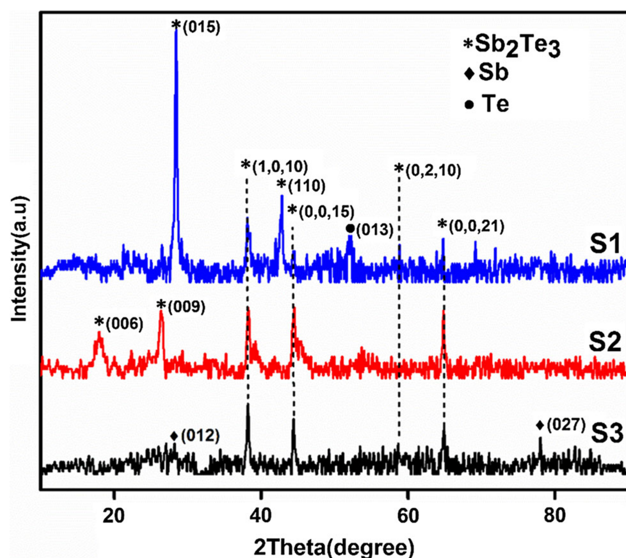

Fig. 3 XRD patterns of the all samples as deposited

belongs to the R$\bar{3}m$ space group of polycrystalline Sb_2Te_3 thin films is acquired [14]. Sample S2 and S3 crystallinity is similar. One difference is that at 2θ of 28.66° and 78.40° in S3 there are peaks corresponding to metallic Sb planes (012) and (027), respectively. This demonstrates that there exists Sb nanocrystals in S3, but not in S2.

For further evidence of the presence of Sb_2Te_3–Sb crystal boundary in S3, the morphology of the sample S3 is characterized by TEM, as shown in Fig. 4a. It illustrates that the sample S3 is polycrystalline nature. The crystal boundaries highlighted by dot line can be attributed to Sb_2Te_3–Sb_2Te_3 or Sb_2Te_3–Sb crystal boundaries. To investigate the microstructural details of the boundaries, high-resolution transmission electron microscopy (HRTEM) analysis is employed, as shown in Fig. 4b. An obvious crystal boundary is between two crystal lattice. The spacing of 0.2133 nm is consistent with the lattice spacing of Sb_2Te_3 (110) plane, while the spacing of 0.1868 nm corresponds to Sb (012) plane. These planes are also seen from XRD patterns. It reveals the existence of Sb_2Te_3–Sb crystal boundary.

The open-circuit voltage (Voc) versus temperature difference (ΔT) in-plane of all samples at room temperature is shown in Fig. 5. From the slopes of the linear fitting (straight lines), the Seebeck coefficients are obtained. The Seebeck coefficient of sample S3 (536 μV K^{-1}, solid square) approximately is six times of that of sample S2 (90 μV K^{-1}, solid rhombus). The results can be supported by the Mott relation [15].

$$S = \frac{\pi^2\kappa_B^2}{3q}T\left\{\frac{d[\ln(\sigma(E))]}{dE}\right\}_{E=E_F} = \frac{\pi^2\kappa_B^2}{3q}T\left\{\frac{dn(E)}{ndE}+\frac{d\mu(E)}{\mu dE}\right\}_{E=E_F}, \quad (1)$$

where κ_B is the Boltzmann constant, T is the absolute temperature, q is the electronic charge, and $\sigma(E) = n(E)q\mu(E)$ is the electrical conductivity, in which $n(E)$ is the carrier concentration, and $\mu(E)$ the carrier mobility depending on energy. It reveals that as the function of the energy derivative of the energy-dependent electrical conductivity at the Fermi (E_F), the Seebeck coefficient is inversely related to carrier concentration and carrier mobility. From Table 1, we know that the carrier concentrations of samples are comparable, but the carrier motilities differ greatly. A decrease of carrier mobility occurs in sample S3 compared to S2. Therefore, the Seebeck coefficient of sample S3 gets remarkably increase in according to Eq. 1. As is known, most insulators have a high Seebeck coefficient but low electrical conductivity. However, our Sb-rich Sb_2Te_3 thin film is not the same as insulators, which do not behave so large carrier concentration.

The decrease of carrier mobility can be attributed to energy potential barrier forming at the Sb–Sb_2Te_3 nanocrystal interfaces (crystal boundaries). The existence of nanocrystals and the Sb–Sb_2Te_3 nanocrystal interfaces can be seen from TEM images and/or XRD patterns. It is demonstrated that nanocomposite materials with proper work function difference could produce energy filtering of carriers effect [6, 16]. The band alignment of Sb and Sb_2Te_3 metal–semiconductor interface is shown in Fig. 6a. Generally, Sb_2Te_3 is a degenerate semiconductor, i.e., the Fermi level (E_F) is positioned inside the valence band [17]. The band gap (Eg), electron affinity (EA), and work function (Φ) of Sb_2Te_3 [18, 19] and Sb nanocrystals are taken from bulk values. The equilibrium band diagram for Sb–Sb_2Te_3 interface is shown in Fig. 6b, indicating the formation of band-bending potential barrier at the

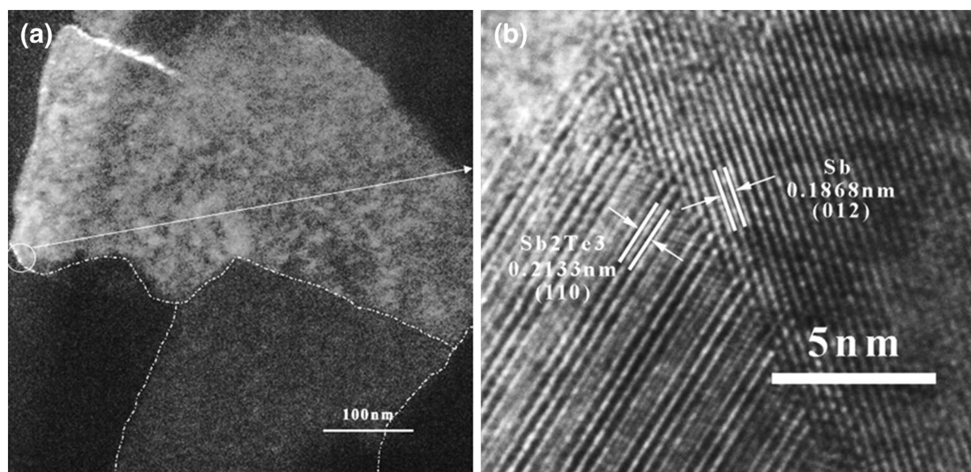

Fig. 4 **a** TEM image of sample S3, and **b** HRTEM image taken from the area designated in (**a**)

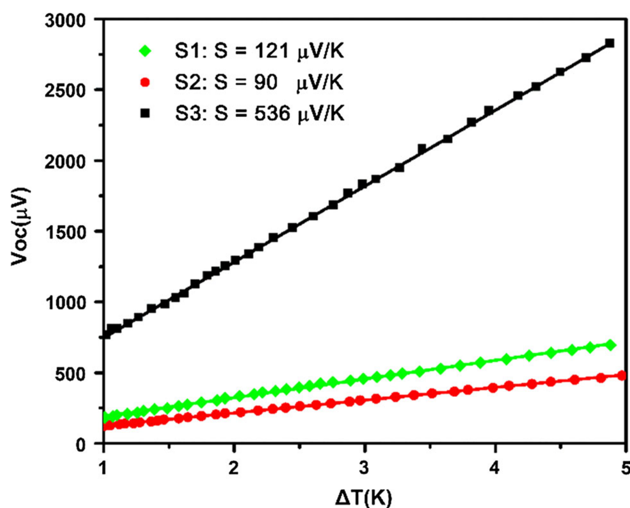

Fig. 5 A plot of open-circuit voltage (Voc) versus temperature difference (ΔT) in-plane for samples measured at room temperature. The *straight lines* are the linear fitting for all measured data. And the *slopes* give the Seebeck coefficient

interface. No interface defect states (causing Fermi level pinning) are assumed.

From the diagram (Fig. 6a) we can see the work function values of Sb and Sb_2Te_3 are 4.55 and 4.45 eV, respectively. Therefore, an upward band bending is created (Fig. 6b). The potential barrier height would be a few ($\sim$0.1) eV, which can effectively filter out low-energy (cold) carriers and let through the high-energy (hot) carriers [6]. At the interfaces, carriers suffer a strong energy dependence scatter, resulting in carrier mobility decrease and separation of hot and cold carriers. It is known that cold carriers are bad for the Seebeck coefficient [20]. Eventually, carriers with high energy can pass the interfaces, while low energy carriers cannot, generating filtering carrier effect. Therefore hot and cold carriers are separated and Seebeck coefficient is enhanced [21–23].

According to theory of heat transport, nanocrystal interfaces may scatter mid- to long-wavelength phonons which transport large fraction of heat [20]. The nanoinclusions have the ability to decrease matrix material thermal conductivity [24]. The measured thermal conductivities in the direction normal (i.e., vertical) to the film surface for different samples are shown in Table 1. Among the samples, S3 has the lowest thermal conductivity of 0.10 W m^{-1} K^{-1}, decrease by 41 % compared with S2. Recently, most methods of thermal conductivity measurement give the thermal conductivity of the samples in the normal direction of the film. The differential 3ω technique we used also like this. However, the electric

Table 1 Summary of in plane Hall mobility μ_H, carrier concentrations n, Hall conductivity σ_H = n q μ_H, conductivity σ_F (measured by Four Probe method), power factor $P = S^2\sigma_H$ and cross plane thermal conductivity κ

Sample	μ_H (cm^2 V^{-1} s^{-1})	N (10^{19} cm^{-3})	σ_H (S cm^{-1})	σ_F (S cm^{-1})	P (μW cm^{-1} K^{-2})	κ (W m^{-1} K^{-1})	ZT
S1	8.7	7.01	97.58	90.76	1.43	0.13	0.33
S2	11.7	7.73	144.71	126.79	1.17	0.17	0.21
S3	0.57	8.03	7.32	7.06	2.10	0.10	0.63
Ref. [11]	9.52	13.0	88.93	–	2.23	–	–

The figure of merit ZT = S^2 σ_HT/κ, T = 300 K

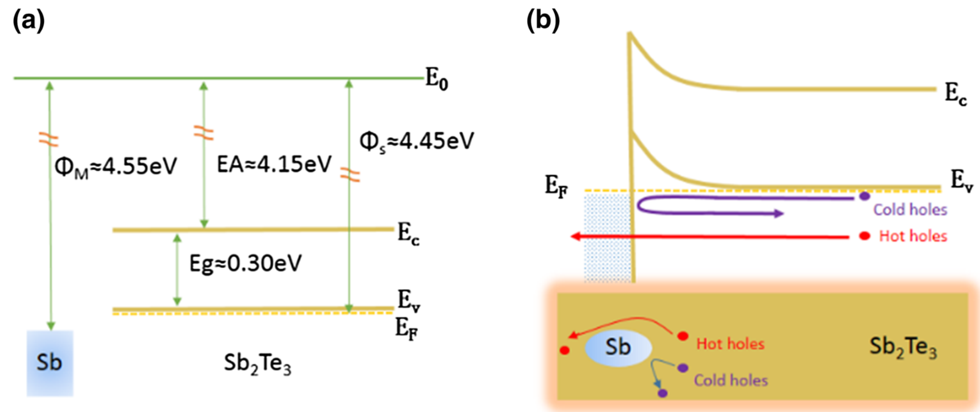

Fig. 6 Band diagram of Sb–Sb_2Te_3 metal–semiconductor interface. **a** Band alignment of Sb–Sb_2Te_3 before contact. **b** Equilibrium band diagram of Sb–Sb_2Te_3 after contact, regardless of interface defect state

properties are acquired in the parallel direction of the films. From the preparation method of our samples, they are all isotropic. Then ZTs gain. ZTs at 300 K shown in Table 1 demonstrates S3 has a maximum value.

4 Conclusion

In summary, antimony tellurium thin films were prepared by co-evaporation of evaporation rate fixed Te and evaporation rate varied Sb elements using a MBE system. Meeting stoichiometric ratio Sb_2Te_3, Sb-rich and Te-rich Sb_2Te_3 thin films were acquired following the evidence of EDS analysis. The XRD patterns demonstrated that diffraction peaks of Sb arose in Sb-rich film. TEM images shown the presence of the crystal boundaries of Sb_2Te_3–Sb, and especially, in HRTEM an obvious crystal boundary of Sb_2Te_3 (110) plane and Sb (012) plane were illustrated in Sb-rich film. Seebeck coefficient measurement revealed that Sb-rich Sb_2Te_3 film held a value of 536 $\mu V\ K^{-1}$ at room temperature, almost six times of stoichiometric Sb_2Te_3 thin film. Through the Hall Effect measurement, we found that the carrier mobility of the Sb-rich Sb_2Te_3 film decreased sharply, whereas the carrier concentration was comparable within all samples.

The significantly enhancement of Seebeck coefficient is attributed to carrier energy filtering effect. In the Sb-rich Sb_2Te_3 thin films, effective potential barriers form at the interfaces of Sb and Sb_2Te_3 nanocrystals. The presence of the potential barrier can essentially filter carriers whose energy is lower than barrier, but hardly influence the carriers with higher energy. Finally, the hot and the cold carriers are separated and the Seebeck coefficient is enhanced. At the same time, the Sb–Sb_2Te_3 interfaces may scatter mid- to long-wavelength phonons and Sb-rich Sb_2Te_3 thin film have a low thermal conductivity illustrated by differential 3ω technique thermal conductivity measurement. Eventually, Sb-rich Sb_2Te_3 thin film behaves an improved ZT. This experiment result implies that by altering Sb content, various Seebeck coefficients would be acquired in Sb-rich Sb_2Te_3 films. The prominent thermopower makes it possible for use to thermo-electric device such as thermoelectric sensor.

Acknowledgments This research was supported by Shanghai Science and Technology Funds (10520710400, 10PJ1403800, 11DZ1111200), Yunnan Provincial Science and Technology Department (2010AD003), National Natural Science Foundation of China (21103104), Innovation Foundation of Shanghai University and the Special Fund for Selection and Cultivation Excellent Youth in the University of Shanghai city. The authors gratefully acknowledge teachers from Instrumental Analysis Research Centre of Shanghai University for his help in XRD, TEM and XPS experiment.

References

1. J. Androulakis, C.H. Lin, H.J. Kong, C. Uher, C.I. Wu, T. Hogan, B.A. Cook, T. Caillat, K.M. Paraskevopoulos, M.G. Kanatzidis, J. Am. Chem. Soc. **129**, 9780–9788 (2007)
2. A.I. Boukai, Y. Bunimovich, J. Tahir-Kheli, J.K. Yu, W.A. Goddard Iii, J.R. Heath, Nature **451**, 168–171 (2008)
3. T.C. Harman, Science **297**, 2229–2232 (2002)
4. X.H. Yang, X.Y. Qin, J. Zhang, D. Li, H.X. Xin, M. Liu, J. Alloys Compd. **558**, 203–211 (2013)
5. J.P. Heremans, V. Jovovic, E.S. Toberer, A. Saramat, K. Kurosaki, A. Charoenphakdee, S. Yamanaka, G.J. Snyder, Science **321**, 554–557 (2008)
6. S. Faleev, F. Léonard, Phys. Rev. B **77**, 214304 (2008)
7. J.P. Heremans, C.M. Thrush, D.T. Morelli, J. Appl. Phys. **98**, 063703 (2005)
8. Z. Xiong, X. Chen, X. Huang, S. Bai, L. Chen, Acta Mater. **58**, 3995–4002 (2010)
9. J.M. Zide, D.O. Klenov, S. Stemmer, A.C. Gossard, G. Zeng, J.E. Bowers, D. Vashaee, A. Shakouri, Appl. Phys. Lett. **87**, 112102 (2005)
10. M.Y. Kim, T.S. Oh, J. Electron. Mater. **38**, 1176–1181 (2009)
11. B. Fang, Z. Zeng, X. Yan, Z. Hu, J. Mater. Sci. Mater. Electron. **24**, 1105–1111 (2013)
12. D.G. Cahill, Rev. Sci. Instrum. **61**, 802 (1990)
13. X. Zheng, L. Qiu, G. Su, D. Tang, Y. Liao, Y. Chen, J. Nanopart. Res. **13**, 6887–6893 (2011)
14. T.B. Chen, P. Fan, Z.H. Zheng, D.P. Zhang, X.M. Cai, G.X. Liang, J.R. Chi, Adv. Mater. Res. **2400**, 194–196 (2011)
15. M. Cutler, N. Mott, Phys. Rev. **181**, 1336–1340 (1969)
16. R. Kim, M.S. Lundstrom, J. Appl. Phys. **111**, 024508 (2012)

17. D.H. Rose, F.S. Hasoon, R.G. Dhere, D.S. Albin, R.M. Ribelin, X.S. Li, Y. Mahathongdy, T.A. Gessert, P. Sheldon, Prog. Photovolt. Res. Appl. **7**, 331–340 (1999)
18. M.A. Matin, M. Mannir Aliyu, A.H. Quadery, N. Amin, Sol. Energy Mater. Sol. Cells **94**, 1496–1500 (2010)
19. G. Hao, X. Qi, G. Wang, X. Peng, S. Chang, X. Wei, J. Zhong, RSC Adv. **2**, 10694 (2012)
20. A. Minnich, M. Dresselhaus, Z. Ren, G. Chen, Energy Environ. Sci. **2**, 466–479 (2009)
21. D.K. Ko, Y. Kang, C.B. Murray, Nano Lett. **11**, 2841–2844 (2011)
22. S. Sumithra, N.J. Takas, D.K. Misra, W.M. Nolting, P.F.P. Poudeu, K.L. Stokes, Adv. Energy Mater. **1**, 1141–1147 (2011)
23. S. Zhang, T. Zhu, S. Yang, C. Yu, X. Zhao, J. Alloys Compd. **499**, 215–220 (2010)
24. X. Cai, Xa Fan, Z. Rong, F. Yang, Z. Gan, G. Li, J. Phys. D Appl. Phys. **47**, 115101 (2014)